IEEE Photonics Journal
An IEEE Photonics Society Publication

Open Access

Scatterometer and Intensity Distribution Meter With Screen Image Synthesis

Volume 12, Number 5, October 2020

Yeh-Wei Yu
Tsung-Hsun Yang
Ching-Cherng Sun
Yun-Hsuan Lin
Ming Le
Chih-Wei Chen
Po-Kai Hsieh
X. H. Lee

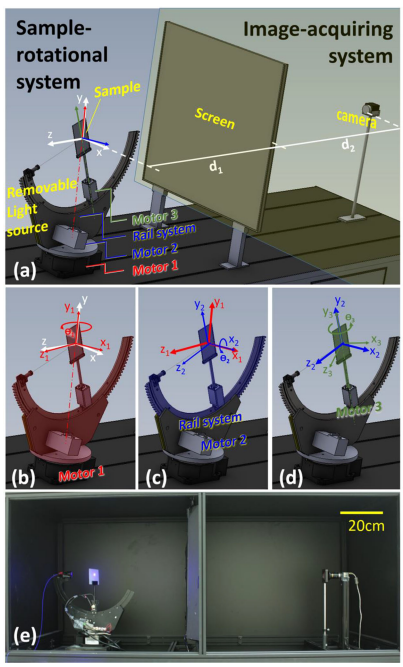

DOI: 10.1109/JPHOT.2020.3025485

IEEE photonics SOCIETY
IEEE

Scatterometer and Intensity Distribution Meter With Screen Image Synthesis

Yeh-Wei Yu, Tsung-Hsun Yang, Ching-Cherng Sun, Yun-Hsuan Lin, Ming Le, Chih-Wei Chen, Po-Kai Hsieh, and X. H. Lee

Department of Optics and Photonics, National Central University, Chung-Li 320, Taiwan

DOI:10.1109/JPHOT.2020.3025485

Manuscript received July 29, 2020; revised September 11, 2020; accepted September 16, 2020. Date of publication September 29, 2020; date of current version October 7, 2020. This work was supported by the Ministry of Science and Technology of Taiwan under Grants MOST 108-2221-E-008 -097 -MY3, 108-2221-E-008-084-MY3, and 108-2221-E-008-092-MY2. Corresponding author: Ching-Cherng Sun. (e-mail: ccsun@dop.ncu.edu.tw).

Abstract: A screen image synthesis (SIS) system is superior than the conventional methods in terms of high-speed measurement and low screen-cross-talk noise when used as a whole-field light-distribution meter. However, reflection signals cannot be measured using the conventional SIS system when it is used as a scattering meter. Furthermore, the conventional SIS system cannot be used to measure a large sample when it is used as an intensity distribution meter. In this study, we devised a rail-based SIS system as long as an image reconstruction algorithm. This would allow whole-field scattering light and intensity distribution measurements for various sample sizes. For this purpose, a versatile instrument was assembled by combining a whole-field intensity distribution meter and a whole-field scattering meter. The results of the experiments confirmed that the measuring time was drastically improved when the proposed instrument was used as a whole-field intensity distribution meter and a whole-field scattering meter. The high normalized cross correlation values of both measurements demonstrated the accuracy and feasibility of the proposed algorithm.

Index Terms: SIS system, screen image synthesis, BSDF, goniophotometer, scatterometer.

1. Introduction

Intensity distribution meters and scatterometers are basic tools for many optical applications such as optical design [1]–[3], optical modelling [4]–[8], building design [9], [10], gloss evaluation [11], [12], color estimation [13], [14], and scattering estimation [15], [16]. A high-speed instrument that combines intensity distribution meters and scatterometers can save time, cost, and space. It thus brings benefits to small and medium-sized R&D companies. Conventional goniophotometers and scatterometers detect data point-by-point, and the process is time consuming [13], [14], [17]–[20]. Whole-field measurements using a goniophotometer and scatterometer could take several hours and days, respectively. Therefore, a fast and versatile measuring instrument is urgently required. In many fields, imaging measurement technology has been applied to improve the intensity distribution measurement and the speed of bidirectional scattering distribution function (BSDF) meters [21]–[33]. Ward presented an elegant system using a hemisphere as a projection surface and a fish-eye lens for capturing images [34], [35]. This provides a snapshot measurement. However, reflection signals from parts of the spherical surface tend to be projected onto other parts of

the spherical surface. The reflection signals' cross-talk induces considerable noise. Therefore, we propose using the screen image synthesis (SIS) technology [36]. In this system, a screen is used to acquire large light distribution fields at the far-field distance. Because only one flat screen is used to collect the light in each shot, cross-talk because of reflection is avoided. We conducted whole-field light-distribution measurements at various solid angles. With this approach, we attained high measuring speeds, high angular resolutions, and low cross-talk noise. However, conventional SIS BSDF meters can only be used to measure the bidirectional transmittance distribution function (BTDF), and not bidirectional reflection distribution function (BRDF). This is because the guiding mirrors block most of the reflection signal and induce a strong shadow effect. Furthermore, in the application of the intensity distribution meter, the sample size could vary from millimetres to meters. Because the far-field distance increases when the sample gets larger, the far-field distance varies from a couple of millimetres to a couple of meters. The angular coverage of the screen decreases when the measuring distance increases. Therefore, if the measuring distance is long, the view-angle interval must be decreased, and the number of shots must be increased. However, the conventional SIS meter lacks a general image reconstruction algorithm for any view-angle interval. In this paper, we used two approaches to assemble a high-speed instrument that combines intensity-distribution meters and scatterometers: (1) We devised a rail-based approach for the SIS system. The rail system was designed to minimize the shadow effect of the automatic measurement system. (2) An image reconstruction algorithm with an adjustable rotational angle was developed. This allowed measurement of the intensity distribution for various sample sizes.

2. The SIS System

2.1. Architecture

Fig. 1 depicts the SIS system. Fig. 1(a) shows that it consists of an image-acquiring system and a sample-rotational system. The image-acquiring system consists of a camera and a screen. The irradiance captured by the CMOS sensor corresponded to the radiance from each position of the screen and was captured by the camera. The camera consists of a CMOS image sensor (IDS GmbH, Germany, UI-2280SE, 2248 $\times$ 2048 pixels, pixel size: 3.45 μm) and a lens (Edmund Optics, USA, Ultrahigh-resolution 5-mm). The screen is a white polymer sheet that is attached to a glass plate with an antireflection coating, and the size of the glass plate is 601 $\times$ 496 $\times$ 3 mm^3. The distance (d_1) between the sample and the screen is 50cm, and the distance (d_2) between the screen and the camera is 75cm. The screen is a heavy scattering transmission film. To check the scattering property of the polymer sheet, it was illuminated by the light with incident angle 0 $^\circ$ and 45 $^\circ$. And the measured intensity distribution is quasi-Lambertian with the FWHM equaling to 115°. Since the ray emitted from the sample impinges the screen within $\pm$38 $^\circ$, and the ray emitted from the screen impinges the camera within $\pm$27.5 $^\circ$, the optical property of the polymer sheet was treated as Lambertian distribution. A Cartesian coordinate system (x, y, and z) is defined in the image-acquiring system. The sample-rotational system is driven using three motors. Motor 1 rotates all components of the sample-rotational system along the red axis. A rail system is fixed on the loading side of Motor 1 and is driven by Motor 2, which rotates the load components along the blue axis. Motor 3 is fixed on the loading side of the rail system, which rotates the sample along the green axis, and it only operates when the instrument functions as a BSDF meter. Fig. 1(b) shows a Cartesian coordinate system defined on the loading side of Motor 1 (x_1, y_1, z_1). When Motor 1 rotates, Motor 2, the rail system and the components loaded by the rail system, rotate θ_1 along the y-axis. Fig. 1(c) shows the Cartesian coordinate system defined on the loading side of the rail system (x_2, y_2, z_2). When Motor 2 rotates, the components on the rail system, including Motor 3, a sample, and a laser light source, rotate θ_2 along the x_1-axis. Fig. 1(d) shows a Cartesian coordinate system defined on the loading side of Motor 3 (x_3, y_3, z_3). When Motor 3 rotates, the sample rotates θ_3 along the y_2-axis. In this study, Motors 1 and 2 rotate the samples through 60 angles, and the image-acquiring system is used to capture the whole-field light distribution. After the progress of parameter optimization and system calibration, the image reconstruction algorithm

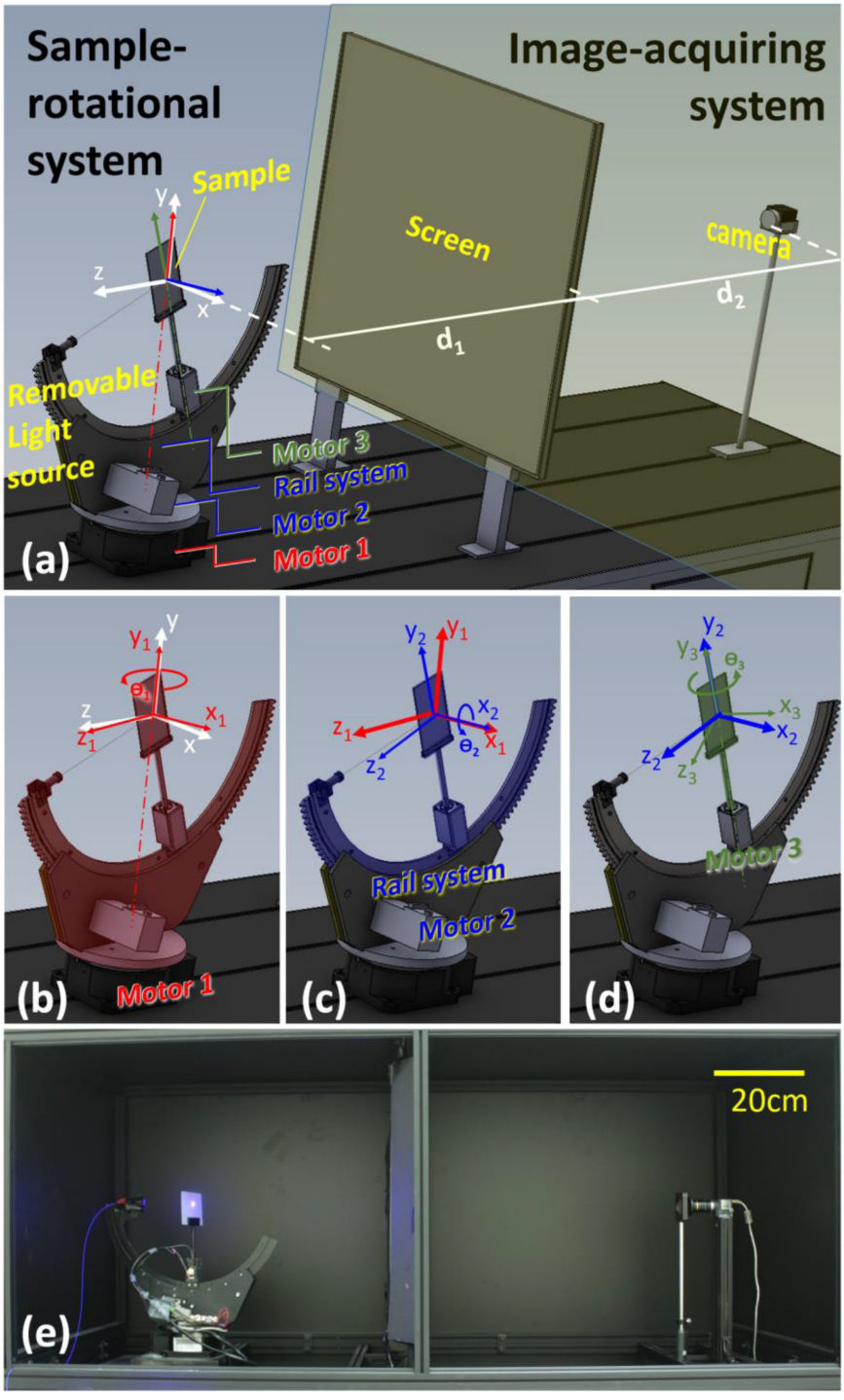

Fig. 1. (a). The tested SIS system is composed of a sample-rotational system and an image-acquiring system. It can be used as an intensity distribution meter or BSDF meter. When it is used as an intensity distribution meter, the removable light source is removed, and Motor 3 is not actuated. When it is used as a BSDF meter, both the light source and Motor 3 are in operation. (b)–(c) show the coordinate system defined on the loading side of Motor 1, Motor 2, and Motor 3, respectively. (d) shows the real system.

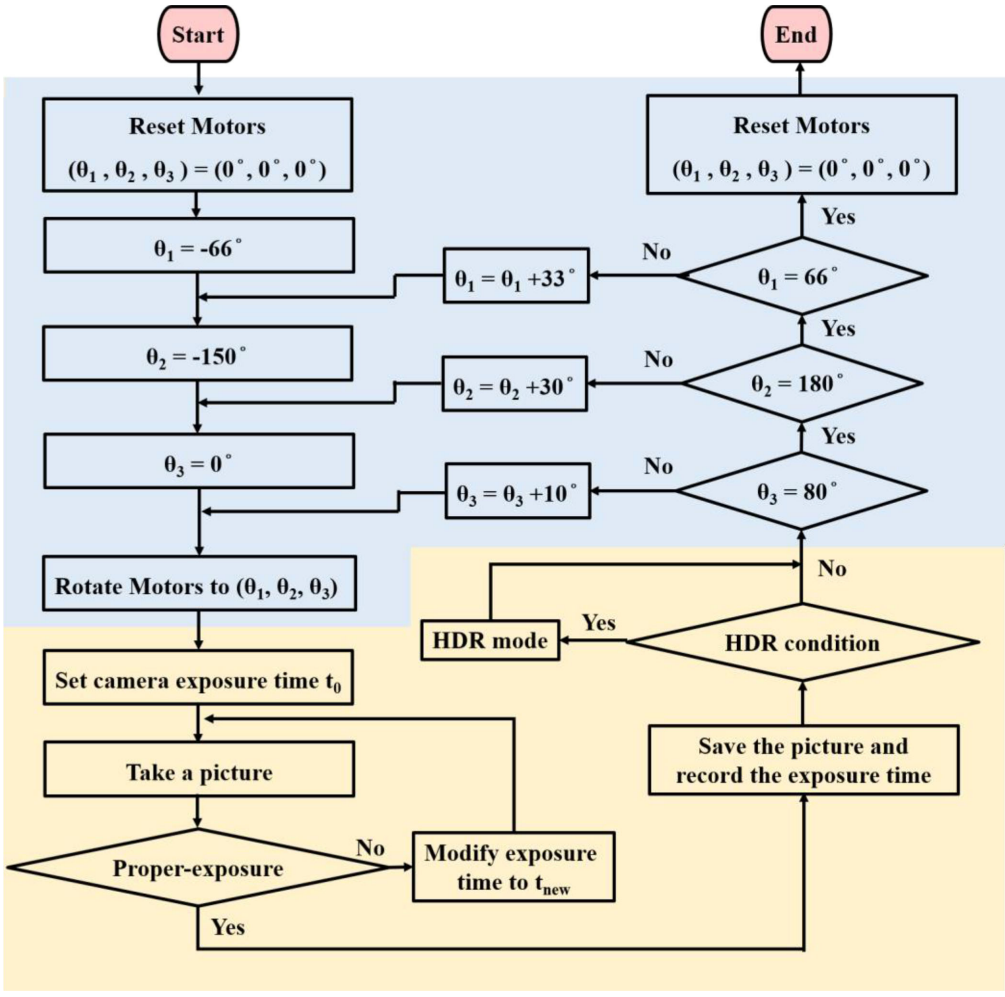

Fig. 2. Automatic measurement process of the SIS system.

is used to obtain the 2-D light distribution. Fig. 1(e) shows the real system, and a scalar bar on the top right side shows the length of 20 cm.

2.2. Automatic Measurement Process

Fig. 2 depicts the automatic measurement process of the SIS system, which consists of motor-controlling (blue part) and camera-controlling processes (yellow part). In the motor-controlling process, three motors are used to rotate the samples to specified angles (θ_1, θ_2, θ_3). Motor 1 and Motor 2 control the view angle between the image-acquiring system and the sample. Motor 1 rotates from $-66°$ to 66° with a step of 33°. Motor 2 rotates from $-150°$ to 180° with a step of 30°. The two motors rotate to 60 angles to cover the 4-π solid angle surrounding the sample. Motor 3 is applied only when the instrument functions as a BSDF meter. This motor is used to control the incident angle of the laser beam, and it rotates from 0° to 80° with a step of 10°.

The camera-controlling process is combined with exposure and high dynamic range (HDR) processes. For the exposure process, the initial exposure time t_0 is guessed based on the measurement experience of similar samples. After a picture is captured, the histogram of the picture is used to evaluate whether it is properly-exposed, i.e., the maximum gray level of the captured

image should be around 80% of the pixel bit depth. If it is properly-exposed, the exposure time is set t_{new}. If it is not, the picture is saved and the exposure time record is renewed. In the HDR process, the application of the HDR technique depends on the rotational angle. If the rotational angle of the sample causes specular reflection to impinge on the screen, then the HDR technique is applied. Generally, the HDR image consists of three pictures. In addition to the exposure time t_{new}, images at $1.5t_{new}$ and $3t_{new}$ are captured. The proper exposure region of each picture is captured, the grey-level of each picture is divided by the corresponding exposure time, and finally, an HDR image is composed. In the HDR image, a ring noise may appear around the specular reflection point. It is caused by the step drop of energy resolution between different exposure periods. Since the irradiance of the noise is around 0.5%∼1% of the strong specular point, it is ignored in this paper.

2.3. Image Reconstruction Algorithm

Considering the light being scattered from the screen following a Lambertian distribution, for a camera lens with a small f-number, the intensity distribution on the screen I (x, y) that corresponds to the irradiance captured on the CMOS sensor E_c (x, y) is expressed as follows [37]:

$$I(x, y) \propto \frac{E_c(x,\ y)}{cos^4\theta_c \cdot cos^3\theta_z}, \tag{1}$$

where θ_z is the zenith angle emitted from the sample with respect to the z-axis

$$\theta_z = \tan^{-1}\left(\frac{\sqrt{x^2 + y^2}}{d_1}\right), \tag{2}$$

and θ_c is the zenith angle with respect to the normal direction of the camera and can be expressed as follows:

$$\theta_c = \tan^{-1}\left(\frac{\sqrt{x^2 + y^2}}{d_2}\right). \tag{3}$$

Because the imaging system is static, the sample is rotated. The calculated intensity is placed in the right-hand position. The Cartesian coordinates attached to the screen, Motor 1, Motor 2, and Motor 3/samples are expressed as the span of the bases B^0, B^0, B^1, and B^2 i.e., $B^0[x\ y\ z]^T$, $B^0[x_1\ y_1\ z_1]^T$, $B^1[x_2\ y_2\ z_2]^T$, and $B^2[x_3\ y_3\ z_3]^T$, respectively. The origin of the coordinate frames is located at the rotational center of the sample. For the rotation of Motors 1, 2, and 3, the rotational matrix is expressed as follows:

$$\left[R^1\right]_{B_0} = \begin{bmatrix} \cos\theta_1 & 0 & \sin\theta_1 \\ 0 & 1 & 0 \\ -\sin\theta_1 & 0 & \cos\theta_1 \end{bmatrix}, \tag{4}$$

$$\left[R^2\right]_{B_1} = \begin{bmatrix} 1 & 0 & 0 \\ 0 & \cos\theta_2 & -\sin\theta_2 \\ 0 & \sin\theta_2 & \cos\theta_2 \end{bmatrix}, \tag{5}$$

and

$$\left[R^3\right]_{B_2} = \begin{bmatrix} \cos\theta_3 & 0 & \sin\theta_3 \\ 0 & 1 & 0 \\ -\sin\theta_3 & 0 & \cos\theta_3 \end{bmatrix}, \tag{6}$$

where the subscripts B_0, B_1, and B_2 indicate that they are used as the basis of the corresponding rotational matrices. Using Eqs. (4)–(6), we apply the change of basis to obtain each rotational matrix with the same basis B_0,

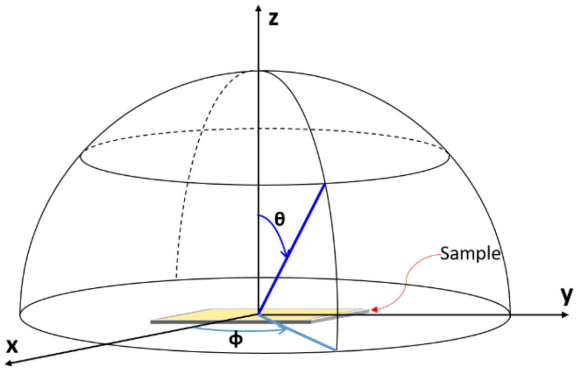

Fig. 3. Light emitted from the sample is expressed in spherical coordinates.

$$\left[R^1\right]_{B_0} = \left[I\right]_{B_0}\left[R^1\right]_{B_0}\left[I\right]_{B_0}, \tag{7}$$

$$\left[R^2\right]_{B_0} = \left[R^1\right]_{B_0}\left[R^2\right]_{B_1}\left[\left(R^1\right)^{-1}\right]_{B_0}, \tag{8}$$

$$\left[R^3\right]_{B_0} = \left[R^1\right]_{B_0}\left[R^2\right]_{B_1}\left[\left(R^1\right)^{-1}\right]_{B_0}\left[R^1\right]_{B_0}\left[R^3\right]_{B_2}\left[\left(R^1\right)^{-1}\right]_{B_0}\left[R^1\right]_{B_0}\left[\left(R^2\right)^{-1}\right]_{B_1}\left[\left(R^1\right)^{-1}\right]_{B_0}, \tag{9}$$

when the sample is rotated by motor 1, motor 2, and motor 3, the transfer matrix becomes

$$\left[R^3\right]_{B_0}\left[R^2\right]_{B_0}\left[R^1\right]_{B_0} = \left[R^1\right]_{B_0}\left[R^2\right]_{B_1}\left[R^3\right]_{B_2}, \tag{10}$$

The intensity distribution captured with the Cartesian coordinates attached to the screen is transferred to the Cartesian coordinates attached to the sample

$$\begin{bmatrix} x_3 \\ y_3 \\ z_3 \end{bmatrix} = \left[R^1\right]_{B_0}\left[R^2\right]_{B_1}\left[R^3\right]_{B_2}\begin{bmatrix} x \\ y \\ z \end{bmatrix}, \tag{11}$$

The Cartesian coordinates are mapped to spherical coordinates (Fig. 3) as follows:

$$\theta = \tan^{-1}\left(\frac{\sqrt{x^2+y^2}}{z}\right), \tag{12}$$

$$\phi = \tan^{-1}\left(\frac{x}{y}\right), \tag{13}$$

After the images for different rotational angles are captured, equation (1) is used to calculate the intensity distribution at θ_1, θ_2, θ_3 (x, y). Subsequently, equations (12)–(13) are used to calculate the intensity at θ_1, θ_2, θ_3 (θ, φ). Generally, 60 pictures with various values of θ_1 and θ_2 are used to reconstruct the whole field distribution of the intensity or CCBSDF with specific $\theta 3$. This is expressed as follows:

$$I_{\theta 3}\ (\theta,\phi) = CCBSDF_{\theta 3}\ \ (\theta,\phi) = \sum_{i=-2}^{2}\sum_{j=-5}^{6}\frac{I_{33i,30j,\theta 3}\,(\theta,\phi)}{\mathrm{W}\,(\theta,\phi)}, \tag{14}$$

where W (θ, φ) is the number of repetitions of the superposition process. It means the final measurement results are all summed together, and is divided by the repetition times. If the measurement results overlap to each other at some angle (θ, φ), I $_{\theta 3}$ will be calculated as the average value.

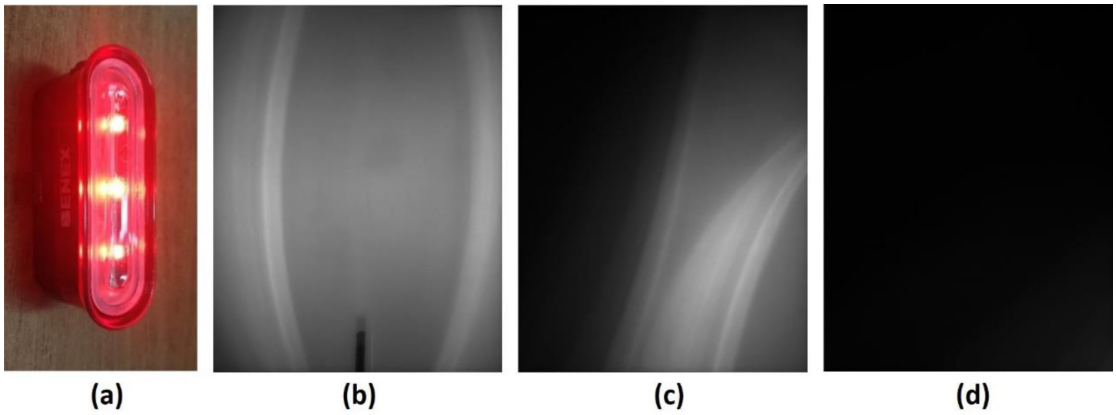

Fig. 4. When the SIS system was used as an intensity distribution meter, (a) commercial bicycle rear light was used as the sample; (b)–(d) captured pictures of $I_{0,0,0}$ (θ, φ), $I_{33,30,0}$ (θ, φ), and $I_{66,60,0}$ (θ, φ), respectively.

3. Experimental Results

3.1. SIS Intensity Distribution Meter

When the proposed instrument was used as an SIS intensity distribution meter, Motor 3 was replaced with a sample mount, and the light source was removed. Aided by the image reconstruction algorithm with an adjustable rotational angle, this system allowed measurement of the intensity distribution of various sample sizes. However, the far-field distance increases when the sample gets larger, and the angular coverage of the screen decreases when the measuring distance increases. This is obtained at the cost of a greater number of shots and leads to a trade-off between the sample size and the measuring time. When the screen size is fixed, the sample size increases and the time consumption (T) depending on the sample size (L) can be roughly expressed as

$$T \propto L^2. \tag{15}$$

Speed enhancement is thus limited as the sample size expands. In addition, the response function of the camera varies with the wavelength of the incident beam; therefore, we need to measure the sample that has an optical spectrum distributed uniformly on the screen. If the optical spectrum of the sample is not uniformly distributed, the measurement would yield an incorrect result. Therefore, a snapshot hyper-spectrum technique should be used to detect the spectrum variation and identify the camera's response function [38]. Since we focus on the improvement of the rail system and the imaging reconstruction, this topic is beyond the scope of this paper, and it will be considered in our future plan.

Fig. 4(a) depicts the use of a commercial rear bicycle light as the sample. The dimensions of the light source were 64.9 mm $\times$ 21.5 mm $\times$ 23.1 mm. When the distance between the screen and the sample (d_s) was 50 cm, the dimension satisfied the far-field criteria [39]. The measurement process is described in Fig. 2, with the exception of θ_3, which is always set as 0. Fig. 4(b–d) depict the captured images of $I_{\theta1,\theta2,0}$ (θ, φ), where (θ_1, θ_2, θ_3) equals (0, 0, 0), (33, 30, 0), and (66, 60, 0), respectively. For the SIS intensity distribution meter with a resolution of 1°, the whole-field measurement can be completed in less than 15 min. Compared with the 8 hours that the goniophotometer requires, the measuring speed for the SIS intensity distribution meter is enhanced by 3200%.

After 60 pictures were captured, we used the measurement result and applied the image reconstruction algorithm described by Eqs. (1) – (6) and Eqs. (11) – (14) to obtain $I_0(\theta, \varphi)$. The azimuthal equidistant projection was used to map I_0 (θ, φ) to the front and rear hemispheres on two plate disks. This correctly expressed the azimuthal distance but reduced the correction of the

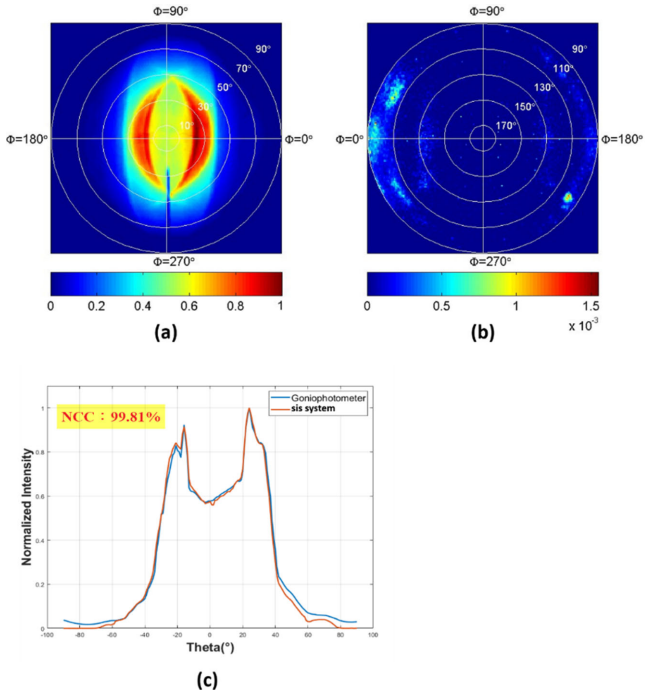

Fig. 5. (a) and (b) Measurement results of the SIS intensity distribution meter applied to the rear light of a commercial bicycle; (c) Comparison of 1-D intensity distribution measurement results obtained using the SIS intensity distribution meter and conventional goniophotometer.

Table 1
NCC for Measured CCBSDF

Incident angle (ϑ_i)	0°	10°	20°	30°	40°	50°	60°	70°	80°
CCBTDF$_{\vartheta i}$	99.87	99.91	99.84	99.88	99.91	99.9	99.84	99.46	96.91
CCBRDF$_{\vartheta i}$	66.94	97.48	93.5	96.18	95.63	90.08	91.1	95.41	98.47

projection area. Fig. 5 illustrates the azimuthal equidistant projection of I_0 (θ, φ). Fig. 5(a) depicts I_0 (θ, φ) on the front hemisphere. The angular resolution of the raw data was 0.06°, which was limited by the image resolution of the camera. We downgraded the angular resolution to 1° to enhance the calculation speed. The clear image demonstrates the precision of the image reconstruction process. A shadow was observed at $\varphi = 270°$ and $25° \leq \theta \leq 90°$. This was caused by the shadow of the rail, and the shadow covered an average of 2.5° of the azimuthal angle. In comparison, the conventional SIS system without the rail system has shadow larger than 10 degrees. And it could easily be removed for the sample with up-down symmetrical optical field. Fig. 5(b) indicates that the detected intensity $I_0(\theta, \varphi)$ on the rear hemisphere was weak, and the maximum normalized intensity was only 1.5×10^{-3}.

Fig. 5(c) depicts a comparison of the 1-D intensity measurement results obtained using the SIS system and a conventional goniophotometer. The blue curve represents the goniometer measurement, and the red curve represents the SIS system measurement. To determine the similarity in the measurement results obtained using the goniometer and SIS system, we applied

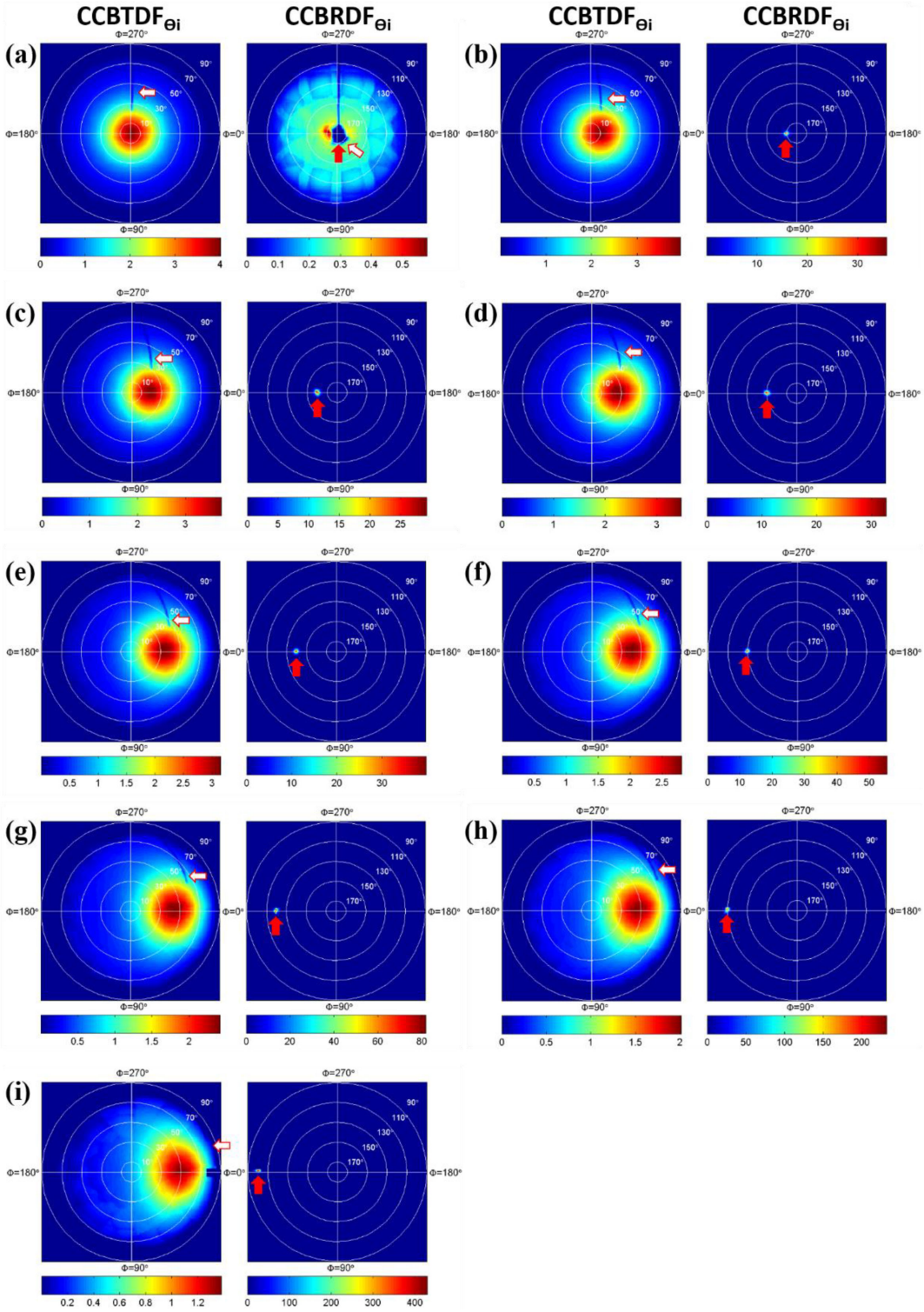

Fig. 6. Measured CCBSDFθi for θi varying from 0° to 80°. The red outlined arrows indicate the observable shadows, and the red solid arrows indicate the position of the specular reflections. (a) when the incident angle is 0°. A shadow of the light source blocks the specular reflection. (b–i) When the incident angle is larger than 10°, the specular reflection is not blocked, and it shows the whole field CCBSDF with negligible shadows.

the normalized cross correlation (NCC) as follows:

$$\mathrm{NCC} = \frac{\sum_n \left[I_{SIS}(\theta_n) - \bar{I}_{SIS}\right] \cdot \left[I_G(\theta_n) - \bar{I}_G\right]}{\sqrt{\sum_n \left[I_{SIS}(\theta_n) - \bar{I}_{SIS}\right]^2 \cdot \sum_n \left[I_G(\theta_n) - \bar{I}_G\right]^2}}, \tag{16}$$

where ISIS and IG are the relative intensity of the SIS system and goniometer, respectively, θ_{n} is the n^{th} angular displacement, and $\bar{\mathrm{I}}_{\mathrm{SIS}}$ and $\bar{\mathrm{I}}_{\mathrm{G}}$ are the mean values of the SIS system and goniometer, respectively. The NCC values were higher than 99.81%, which demonstrates the high accuracy of the SIS intensity distribution meter.

3.2. SIS BSDF Meter

The CCBSDF is a function used to describe scattering and is defined as follows:

$$CCBSDF = \cos\theta_s \cdot BSDF, \tag{17}$$

$$BSDF\ (\theta_i, \phi_i, \theta_s, \phi_s) = \frac{dL_s(\theta_s, \phi_s)}{dE_i(\theta_i, \phi_i)}, \tag{18}$$

where the terms $(\theta_{\mathrm{i}}, \phi_{\mathrm{i}})$ and $(\theta_{\mathrm{s}}, \phi_{\mathrm{s}})$ are the incident and scattering direction angles, respectively, relative to the surface normal [37], [40]. $\mathrm{L_s}$ is the radiance distribution of the scattering light, and $\mathrm{E_i}$ is the irradiance distribution of the incident light. The CCBSDF indicates the intensity distribution of the diffuser. When the instrument functions as an SIS BSDF meter, a 450-nm wavelength laser was coupled to a multimode fibre and transmitted to one end of the rail system. A spherical lens (focal length: 20 mm) transferred the outcoupled laser beam to form an illumination beam with a 1-cm diameter.

A diffuser plate was used as the sample. Motor 3 was used to change the incident angle (θ_{i}) from 0° to 80°. Here, 60 pictures were captured at each incident angle. Therefore, for nine incident angles, 540 pictures were captured. We applied the image reconstruction algorithm described by Eq.(1) - (11) to reconstruct the $\mathrm{CCBSDF}_{\theta \mathrm{i}}(\theta, \varphi)$. Fig. 6 (a–i) shows the azimuthal equidistant projection of the $\mathrm{CCBSDF}_{\theta \mathrm{i}}(\theta, \varphi)$ for θ_i changing from 0° to 80°. Each picture contained the cosine-corrected BTDF (CCBTDF, front side hemisphere) and cosine corrected BRDF (CCBRDF, rear hemisphere). The angular resolution was 1°. We use red outline arrows to point out the observable shadows and use red solid arrows to indicate the position of the specular reflections. The CCBRDF in Fig. 6(a) depicts a shadow of the light source, and it blocks the specular reflection. It also displays some non-uniform patterns in the weak-signal region. This is caused by noise at the edge of the screen. Because Eq. (1) and Eq. (2) amplify the noise at the edge of the screen, when the scattering signal is weak, the amplified noise will be observed. If specular reflection dominates the estimation result, it can be ignored in some applications [9]–[12]. If the noise becomes non-negligible, either of two approaches can be used to improve the situation: (1) increase the exposure time of each picture to suppress the noise or (2) decrease the effective area of the screen and increase the shot numbers, thus decreasing the amplification ratio at the edge of the screen. Both methods lead to extended measuring times, and thus limit the speed enhancement.

Fig. 6 (b–i) confirms that, when the incident angle is larger than 10°, the specular reflection is not blocked, and the shadow in the $\mathrm{CCBRDF}_{\theta 3}$ can be ignored because of the weak signal compared with the strong specular reflection. The requirement of measurement resolution is always depended on the applications. For BSDF measurement, 2.5° shadow is negligible, if it doesn't block the specular signal. And it could easily be removed for the sample with up-down symmetrical scattering distribution. The strong specular reflection peak always requires a high-dynamic-range image sensor. Therefore, the HDR technique was applied to enlarge the dynamic range of the acquired image. The NCC results obtained using the SIS system and the conventional goniophotometer for 1-D $\mathrm{CCBSDF}_{\theta i}$ measurement are listed in Table 1. Excepting the CCBRDF_0 at the 0° incident angle, all the NCC values of the $\mathrm{CCBRDF}_{\theta i}$ were higher than 90%. This demonstrates the accuracy and feasibility of the proposed algorithm. The CCBSDF required less than 50 min to complete this

process with eight incident angles (0–80). In contrast, the conventional scatterometer using the goniometer architecture may require 64 hours to obtain data of the same resolution. The measuring speed was enhanced by 7280%.

4. Conclusion

The SIS system exhibits superiority in terms of high-speed measurement and low screen-cross-talk noise. However, the conventional SIS system failed in both reflection signal measurement and large sample measurements. In this study, we improved the SIS system by devising a rail system, which generated a small shadow in both BSDF and intensity distribution measurements. Furthermore, an image reconstruction algorithm with an adjustable rotational angle allowed measurement of the intensity distribution for various sample sizes. Thus, an SIS intensity distribution meter and an SIS BSDF meter were combined to develop a versatile instrument. When the sample size becomes larger or the signal becomes weaker, we should either increase the total shot number or increase the exposure time to improve the measurement precision. This sets a limit on speed enhancement.

When the instrument was used as an SIS intensity distribution meter, Motors 1 and 2 rotated the sample to 60 different angles and allowed the imaging system to acquire the intensity distribution with a 4-π solid angle. Whole-field measurements required 15 min at a resolution of 1° with the proposed approach. Compared to the 8 hours required with a goniophotometer, the measuring speed was enhanced by 3200%. The clear image obtained using the proposed approach confirmed the precision of the image reconstruction process. The average azimuthal width of the shadow was 2.5°. NCC values of 99.81% were achieved between the SIS intensity distribution meter and the conventional goniophotometer, which demonstrates the high accuracy of the SIS intensity distribution meter.

When the proposed instrument was used as an SIS BSDF meter, Motor 3 was used to change the incident angle. By combining 60 pictures from each incident angle, 540 pictures were acquired. The instrument required 50 min for whole-field measurements at a resolution of 1°. Compared to the conventional scatterometer, which uses the goniometer architecture and requires 64 hours, the measuring speed was enhanced by 7280%. The NCC values of the $\mathrm{CCBTDF}_{\theta \mathrm{i}}$ were always higher than 96.91%. The NCC values of the $\mathrm{CCBRDF}_{\theta \mathrm{i}}$ except for the 0° incidence angle case, were higher than 90%. This demonstrates the accuracy and feasibility of the proposed algorithm.

Acknowledgements

The authors would like to thank Chao-Chuan Chen and Denny Peng for their assistance with this study.

References

[1] P. C Acuna, S. Leyre, I Audenaert, Y. Meuret, G. Deconinck, and P. Hanselaer, "Impact of the geometrical and optical parameters on the performance of a cylindrical remote phosphor LED," *IEEE Photon. J.*, vol. 7, no. 5, pp. 1–14, Aug. 2015.
[2] J. Ryckaert *et al.*, "Selecting the optimal synthesis parameters of InP/CdxZn1−xSe quantum dots for a hybrid remote phosphor white LED for general lighting applications," *Opt. Express*, vol. 25, no. 24, pp. A1009–A1022, Oct. 2017.
[3] S. Chang, J. B. Yoon, H. Kim, J. J. Kim, B. K. Lee, and D. H. Shin, "Microlens array diffuser for a light-emitting diode backlight system," *Opt. Lett.*, vol. 31, no. 20, pp. 3016–3018, Oct. 2006.
[4] P. Acuña, S. Leyre, J. Audenaert, Y. Meuret, G. Deconinck, and P. Hanselaer, "Power and photon budget of a remote phosphor LED module," *Opt. Express*, vol. 22, no. s4, pp. A1079–A1092, Jun. 2014.
[5] J. F. Murray-Coleman and A. M. Smith, "The automated measurement of BRDFs and their application to luminaire modelling," *J. Illum. Eng. Soc.*, vol. 19, no. 1, pp. 87–99, 1990.
[6] W. T. Chien, C. C. Sun, and I. Moreno, "Precise optical model of multi-chip white LEDs," *Opt. Express*, vol. 15, no. 12, pp. 7572–7577, Jun. 2007.
[7] I. Moreno and C. C. Sun, "Modeling the radiation pattern of LEDs," *Opt. Express*, vol. 16, no. 3, pp. 1808–1819, Feb. 2008.
[8] J. Audenaert, G. Durinck, F. B. Leloup, G. Deconinck, and P. Hanselaer, "Simulating the spatial luminance distribution of planar light sources by sampling of ray files," *Opt. Express*, vol. 21, no. 20, pp. 24099–24111, Oct. 2013.

[9] E. S. Lee, D. Geisler-Moroder, and G. Ward, "Modeling the direct sun component in buildings using matrix algebraic approaches: Methods and validation," *Sol. Energy*, vol. 160, pp. 380–395, Jan. 2018.
[10] T. Kazanasmaz, L. O. Grobe, C. Bauer, M. Krehel, and S. Wittkopf, "Three approaches to optimize optical properties and size of a South-facing window for spatial Daylight Autonomy," *Build. Environ.*, vol. 102, pp. 243–256, Jun. 2016.
[11] F. B. Leloup, M. R. Pointer, P. Dutré, and P. Hanselaer, "Overall gloss evaluation in the presence of multiple cues to surface glossiness," *J. Opt. Soc. Am. A*, vol. 29, no. 6, pp. 105–1114, Jun. 2012.
[12] F. B. Leloup, G. Obein, M. R. Pointer, and P. Hanselaer, "Toward the soft metrology of surface gloss: A review," *Color Res. Appl.*, vol. 39, no. 6, pp. 559–570, Dec. 2014.
[13] V. G. W. Harrison, "A goniophotometer for gloss and colour measurements," *J. Sci. Instrum.*, vol. 24, no. 1, pp. 21–24, Jan. 1947.
[14] V. A. Jacobs, J. Audenaert, J. Bleumers, G. Durinck, P. Rombauts, and P. Hanselaer, "Rayfiles including spectral and colorimetric information," *Opt. Express*, vol. 23, no. 7, pp. A361–A370, Apr. 2015.
[15] S. Leyre *et al.*, "Determination of the bulk scattering parameters of diffusing materials," *Appl. Opt.*, vol. 52, no. 18, pp. 4083–4090, Jun. 2013.
[16] S. Leyre, Y. Meuret, G. Durinck, J. Hofkens, G. Deconinck, and P. Hanselaer, "Estimation of the effective phase function of bulk diffusing materials with the inverse adding-doubling method," *Appl. Opt.*, vol. 53, no. 10, pp. 2117–2125, Apr. 2014.
[17] D. Hünerhoff, U. Grusemann, and A. Höpe, "New robot-based gonioreflectometer for measuring spectral diffuse reflection," *Metrologia*, vol. 43, no. 2, pp. S11–S16, Mar. 2006.
[18] G. Obein, R. Bousquet, and M. E. Nadal, "New NIST reference goniospectrometer," *Proc. SPIE*, vol. 5880, pp. 241–250, 2005.
[19] A. M. Rabal *et al.*, "Automatic gonio-spectrophotometer for the absolute measurement of the spectral BRDF at in- and out-of-plane and retroreflection geometries," *Metrologia*, vol. 49, no. 3, pp. 213–223, Jun. 2012.
[20] F. B. Leloup, S. Forment, P. Dutré, M. R. Pointer, and P. Hanselaer, "Design of an instrument for measuring the spectral bidirectional scatter distribution function," *Appl. Opt.*, vol. 47, no. 29, pp. 5454–5467, Oct. 2008.
[21] C. de Wasseige, and P. Defourny, "Retrieval of tropical forest structure characteristics from bi-directional reflectance of SPOT images," *Remote Sens. Environ.*, vol. 83, no. 3, pp. 362–375, Dec. 2002.
[22] M. Papas, K. de Mesa, and H. W. Jensen, "A physically-based BSDF for modeling the appearance of paper," *Comput. Graph. Forum*, vol. 33, no. 4, pp. 133–142, Jul. 2014.
[23] M. E. Becker, "Display reflectance: Basics, measurement, and rating," *J. Soc. Inf. Disp.*, vol. 14, no. 11, pp. 1003–1017, Oct. 2006.
[24] J. C. Jonsson, M. D. Rubin, A. M. Nilsson, A. Jonsson, and A. Roos, "Optical characterization of fritted glass for architectural applications," *Opt. Mater.*, vol. 31, no. 6, pp. 949–958, Apr. 2009.
[25] A. Mazikowski and M. Trojanowski, "Measurements of spectral spatial distribution of scattering materials for rear projection screens used in virtual reality systems," *Metrol. Meas. Syst.*, vol. 20, no. 3, pp. 443–452, Sep. 2013.
[26] R. M. Springer, M. E. Thomas, and R. I. Joseph, "Analysis and comparison of single-crystal and polycrystalline Nd:YAG. Scatter," *IEEE J. Quantum Electron.*, vol. 51, no. 8, pp. 1–8, Aug. 2015.
[27] A. Katsifaraki, B. Bueno, and T. E. Kuhn, "A daylight optimized simulation-based shading controller for venetian blinds," *Build. Environ.*, vol. 126, no. 126, pp. 207–220, Dec. 2017.
[28] H. H. P. Wu, Y. P. Lee, and S. H. Chang, "Fast measurement of automotive headlamps based on high dynamic range imaging," *Appl. Opt.*, vol. 51, no. 28, pp. 6870–6880, Sep. 2012.
[29] T. Kruisselbrink, M. Aries, and A. Rosemann, "A practical device for measuring the luminance distribution," *Int. J. Sustain. Light*, vol. 36, no. 1, pp. 75–90, Jun. 2017.
[30] M. Inanici and J. Galvin, "Evaluation of high dynamic range photography as a luminance data acquisition system," *Light. Res. Technol.*, vol. 38, no. 2, pp. 123–136, Aug. 2006.
[31] E. Berrocal, D. L. Sedarsky, M. E. Paciaroni, I. V. Meglinski, and M. A. Linne, "Laser light scattering in turbid media Part I: Experimental and simulated results for the spatial intensity distribution," *Opt. Express*, vol. 15, no. 17, pp. 10649–10665, Aug. 2007.
[32] K. Tohsing, M. Schrempf, S. Riechelmann, H. Schilke, and G. Seckmeyer, "Measuring high-resolution sky luminance distributions with a CCD camera," *Appl. Opt.*, vol. 52, no. 8, pp. 1564–1573, Mar. 2013.
[33] O. Moreau, J. N. Curt, and T. Leroux, "Fast contrast vs. viewing angle measurements for LCDs," in *Proc. EURODIS-PLAY'93*, 1993, pp. 447–449.
[34] G. J. Ward, "Measuring and modeling anisotropic reflection," *Comput. Graph.*, vol. 26, no. 2, pp. 265–272, Jul. 1992.
[35] H. Kostal, D. Kreysar, and R. Rykowski, "Application of imaging sphere for BSDF measurements of arbitrary materials," in *Proc. OSA Front. Opt. Conf.*, 2008, Paper FMJ6.
[36] Y. W. Yu *et al.*, "Bidirectional scattering distribution function by screen imaging synthesis," *Opt. Express*, vol. 20, no. 2, pp. 1268–1280, Jan. 2012.
[37] V. N. Mahajan, *Optical Imaging and Aberrations: Part I. Ray Geometrical Optics*. Bellingham, WA, USA: SPIE, 1998.
[38] C. C. Sun, Y. W. Yu, T. W. Lin, and C. C. Lin, "Detecting system," U.S. Patent, US9574940, 2017.
[39] C. C. Sun, T. X. Lee, S. H. Ma, Y. L. Lee, and S. M. Huang, "Precise optical modeling for LED lighting verified by cross correlation in the midfield region," *Opt. Lett.*, vol. 31, no. 14, pp. 2193–2195, Jul. 2006.
[40] J. C. Stover, *Optical Scattering Measurement and Analysis*. Bellingham, WA, USA: SPIE, 2012.